Check for updates

Advanced Energy Materials

ADVANCED ENERGY MATERIALS
www.advenergymat.de

RESEARCH ARTICLE OPEN ACCESS

A Quantitative Lithium Inventory Framework for Anode-Free Lithium Metal Batteries

Wurigumula Bao[1] | Alex Liu[2] | Thomas S. Marchese[1] | Yuanlong Bill Zheng[1] | Weikang Li[2] | Dhevathi Rajan Rajagopalan Kannan[3] | Vallabha Rao Rikka[3] | Vinay Premnath[3] | Judith Jeevarajan[3] | Ying Shirley Meng[1,2]

[1]Pritzker School of Molecular Engineering, University of Chicago, Chicago, Illinois, USA | [2]Aiiso Yufeng Li Family Department of Chemical and Nano Engineering, University of California, San Diego, California, USA | [3]Underwriters Laboratories Research Institutes, Electrochemical Safety Research Institute, Houston, Texas, USA

Correspondence: Wurigumula Bao (wubao@uchicago.edu) | Ying Shirley Meng (shirleymeng@uchicago.edu)

Received: 31 January 2026 | **Revised:** 13 April 2026 | **Accepted:** 21 April 2026

Keywords: Li inventory quantification | Lithium metal battery | solid electrolyte interface | titration gas chromatography

ABSTRACT

Lithium (Li) metal batteries, with their substantially higher specific capacity, have the potential to nearly double the gravimetric energy density of conventional Li-ion cells, enabling applications that demand exceptional energy-to-weight ratios, including electric vehicles, electric vertical takeoff and landing aircraft (eVTOL), and humanoid robots. However, capacity declines arising from Li inventory imbalance, together with safety concerns under extended cycle life, remain major barriers to their practical deployment. A unified and quantitative understanding of how Li redistributes among the cathode, anode, and electrolyte during operation is still lacking. In this work, we use anode-free batteries as a model system and quantitatively track the Li inventory by combining structural, chemical, and electrochemical analyses. By closing the Li mass balance across multiple cycling stages, we identify three main characteristic regimes of Li evolution and resolve the dominant loss pathways associated with each regime. The resulting Li-inventory framework clarifies the interplay among cathode lattice Li, inactive Li accumulation, and electrolyte depletion, and identifies cathode optimization as a central design requirement for anode-free batteries. In addition, the stage-resolved quantitative dataset generated here provides a structured source of mechanistic insight that can support future data-driven and physics-informed modeling efforts.

1 | Introduction

Lithium-ion batteries (LIBs) have been widely used in electronic devices since 1991 [1], and tremendous progress has been made in improving energy density and reducing cost over the past decades, which allowed them to be incorporated into electric vehicles and grid energy storage as well as for marine and space power systems. Nevertheless, the graphite anode fundamentally limits further increases in energy density. Lithium-metal (Li-metal) anode, featuring negative redox potential (−3.04 V vs. Standard Hydrogen Electrode), lightweight (0.534 g·cm^{-3}), and high theoretical capacity (3860 mAh·g^{-1}), offers a promising pathway to break this limitation and substantially boost the energy density of Li-based batteries [2, 3]. In particular, configurations that utilize no excess Li metal prior to cycling—commonly referred to as anode-free Li-metal batteries at pristine state—show even greater potential for enhanced volumetric energy density [4].

Despite these advantages, both Li-metal and anode-free cells face longstanding challenges, including poor cycle stability and safety concerns arising from dendrite formation, dead Li accumulation,

This is an open access article under the terms of the Creative Commons Attribution License, which permits use, distribution and reproduction in any medium, provided the original work is properly cited.
© 2026 The Author(s). *Advanced Energy Materials* published by Wiley-VCH GmbH

and parasitic interfacial reactions [5, 6]. During cycling, Li^+ ions migrate from the cathode (active Li) to the bare copper current collector and undergo reduction at the surface. Some of the incoming Li^+ is consumed to form the solid electrolyte interphase (SEI Li), while the rest is reduced to metallic lithium that initially remains electrochemically active. Over repeated cycles, however, part of this metallic Li becomes electronically isolated by the evolving SEI, turning into inactive metallic lithium (inactive Li^0) and losing reversibility. Concurrently, some lithium remains trapped in the cathode as residual lattice Li due to cutoff voltages and sluggish kinetics, while interphase formation on the cathode side further consumes lithium to form cathode electrolyte interphase (CEI Li^+). These processes also progressively deplete Li^+ in the electrolyte [7–10]. This dynamic redistribution of lithium involves both reversible and irreversible pathways, and identifying the dominant irreversible processes is essential for improving anode-free cell performance.

Building on this understanding of lithium redistribution, extensive efforts have been devoted to elucidating the failure mechanisms of lithium metal batteries. Loss of active Li—arising from solid electrolyte interphase (SEI) growth and the formation of electronically isolated metallic Li^0—is closely tied to coulombic efficiency (CE) [11]. Consequently, accurately detecting and quantifying SEI Li and inactive Li^0 has been a central focus in diagnosing capacity decay. Paolella et al. employed in situ X-ray diffraction to investigate the degradation mechanisms in NMC 811||Cu cells, reporting inactive Li even at the end of the first discharge at a C/24 rate, with its continued increase with cycling [12]. Hu et al. applied in situ electron paramagnetic resonance imaging (EPRI) to monitor Li plating/stripping behaviors in $LiCoO_2$||Cu cells, revealing uneven and sometimes excessive Li deposition during plating, which promoted inactive Li formation upon stripping. Inactive Li microstructures became smaller and more heterogeneous with cycling, semi-quantifying inactive Li to ~35% of the initially plated Li after five cycles [13]. Grey et al. used in situ ^{7}Li NMR to quantify inactive Li in $LiFePO_4$||Cu cells across different electrolytes, and estimated SEI formation based on CE, highlighting that active Li dissolution remains a major challenge in Li-metal systems and is strongly associated with ongoing SEI growth [8, 14].

While most mechanistic studies of anode-free cells were primarily focused on the anode, several pioneering investigations have highlighted that cross-talk between the cathode and the anode can also profoundly influence cell performance. Winter et al. demonstrated that Li-metal plating morphology varies markedly with the choice of cathode, attributing these differences to transition-metal dissolution behaviors. Specifically, Mn dissolution from $LiNi_{0.5}Mn_{1.5}O_4$ cathodes in the electrolyte leads to spherical Li deposits on Cu foil, while nodule-like Li deposits form on Cu when paired with $LiFePO_4$ and $LiNi_{0.6}Mn_{0.2}Co_{0.2}O_2$ cathodes [15]. Hwang et al. integrated both half-cell and full-cell electrochemical analyses to quantify Li inventory in $LiNi_{1/3}Co_{1/3}Mn_{1/3}O_2$||Cu systems, revealing that capacity loss in early cycles is mainly governed by cathode contributions, while inactive Li^0 formation and SEI growth dominate at later stages [16]. Liaw and co-workers applied the Galvanostatic Intermittent Titration Technique (GITT) to track Li inventory through the cathode active materials utilization coefficient (U), which is crucial for indicating the battery's end-of-life [17]. Furthermore, Dahn and his team employed NMR to quantify electrolyte consumption during cycling in $LiNi_{0.5}Mn_{0.3}Co_{0.2}O_2$(NMC 532)||Cu cells, showing that Li-electrolyte reactions involving salt consumption promote dense Li deposition. As cycling proceeds, depletion of these salt species results in increasingly irregular Li morphology and accelerated electrolyte degradation, ultimately leading to capacity fade [5].

The pioneering studies described above have significantly advanced the qualitative understanding of anode-free Li-metal battery failure. However, a comprehensive and quantitative analysis of capacity loss—one that accounts for all lithium-containing components in the full cell—remains largely unexplored. Such quantitative insight is essential for identifying the most critical loss pathways and for guiding the design of next-generation anode-free systems. In this work, we address this gap by developing a complete analytical framework for quantifying the Li inventory in $LiNi_{0.6}Mn_{0.2}Co_{0.2}O_2$ (NMC 622)||Cu anode-free pouch cell. Six types of Li inventories are quantified using a combination of Titration Gas Chromatography (TGC), Inductively Coupled Plasma Mass Spectrometry (ICP-MS), and X-ray Diffraction (XRD) located at the anode, electrolyte, and cathode, respectively. This unified approach enables quantitative tracking of reversible and irreversible lithium reservoirs, allowing us to elucidate the detailed failure mechanisms governing anode-free Li-metal batteries. Our work sheds light on advanced lithium-based batteries, offering insights that can be applied to other chemistries and accelerate mechanistic studies, ultimately advancing the commercialization of lithium metal batteries.

2 | Results and Discussion

2.1 | Electrochemical Performance Evaluation

Pouch cells were prepared using 3 $mAh{\cdot}cm^{-2}$ NMC 622 as the cathode, Cu (>99.8%, 10 um) as the anode current collector, and Localized High Concentration Electrolyte (LHCE) (4.7 M LiFSI + 2.3 M LiTFSI in DME) as the electrolyte. The cycling performance is shown in Figure 1a. All cells were cycled at charge and discharge rates of C/10-C/10 for two formation cycles and then C/10-C/3 rates for the following cycles with the voltage range of 3–4.3 V under 350 kPa. The cells show the first discharge capacity of 0.23 Ah and 87% as the initial coulombic efficiency (ICE). The average CE of 45 cycles is 99.13%, and the capacity retention is 76.52%. An additional cycle with C/10 charge and discharge was performed, as shown in the orange line (46th cycle) in Figure 1b. This extra cycle avoided the kinetic effect due to the different charge/discharge rates. Interestingly, CE values exceeding 100% were observed during cycling, which indicates the presence of an active metallic Li reservoir on the anode surface. This behavior arises from cathode rate limitations, where lithium plated during charging cannot be fully reintegrated into the cathode under C/3 conditions [18, 19].

Figure 1a shows the Li inventory distribution schematic of the cell before and after cycling. Lithium exists in the cathode structure and the electrolyte salt prior to any electrochemical cycling. Upon the charging process, on the cathode side, partially active Li de-intercalates from the cathode and moves to the anode, while the electrolyte gets oxidized and forms the CEI layer on the cathode

16146840, 0, Downloaded from https://advanced.onlinelibrary.wiley.com/doi/10.1002/aenm.71028 by University Of Chicago Library, Wiley Online Library on [06/05/2026]. See the Terms and Conditions (https://onlinelibrary.wiley.com/terms-and-conditions) on Wiley Online Library for rules of use; OA articles are governed by the applicable Creative Commons License

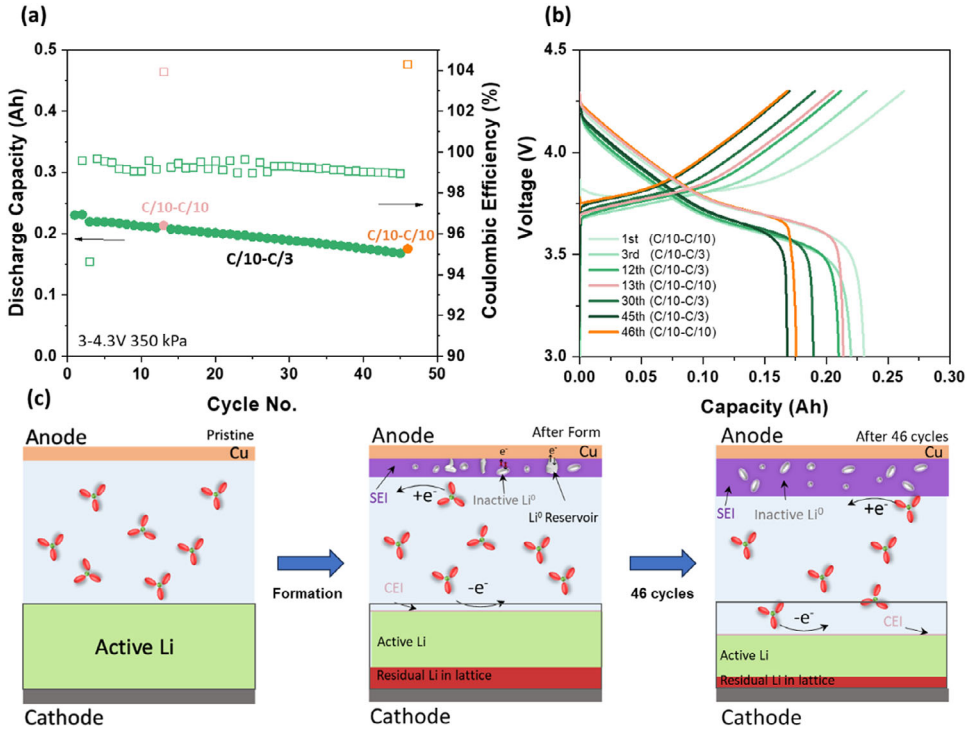

FIGURE 1 | (a) Cycling performance and (b) Charge and discharge voltage profile of NMC 622 || anode-free pouch cell with LHCE electrolyte. (c) Schematic of Li inventory in anode-free cells.

surface simultaneously. On the anode side, the active Li from the cathode and electrolyte will contribute to the Li plating and SEI formation, respectively. During the discharge process, partial Li on the anode will be reversibly stripped and migrate back to the cathode, and the remaining Li will be present as inactive Li^0, SEI, and active Li^0, which occurs in the early cycles due to kinetic limitations of the NMC622 cathode [20]. At the discharge state, Li inventory distribution can be summarized as follows:

$$\begin{aligned} &Li^+ \text{ (pristine cathode)} + Li^+ \text{ (pristine electrolyte)} \\ &= Li^+ \text{ (cycled cathode)} + Li^+ \text{(CEI)} + \text{ Li } \left(\text{inactive } Li^0\right) \\ &+ Li^+ \text{ (SEI)} + Li^+ \text{(cycled electrolyte)} + Li^0 \left(\text{active } Li^0\right) \end{aligned} \quad (1)$$

Here, the TGC method developed previously can quantify the inactive active Li^0 amount [11]. ICP-MS measures the Li^+ concentration in electrolytes and the active Li^0 [21]. Transmission electron microscopy (TEM) helps estimate the CEI amount. Therefore, by establishing the quantification methodology for the cathode, the Li^+ in SEI can be resolved.

2.2 | Quantification of Li Inventory in the Cathode

The correlation between lithium content and lattice parameters in layered NMC cathodes is well established through decades of in situ and operando XRD studies. Wang et al. demonstrated using in situ neutron diffraction that the NMC lattice parameters evolve systematically and reversibly during lithium extraction and reinsertion, with parameter *c* expanding and *a* contracting upon charging [22]. Subsequent operando synchrotron XRD studies of NMC622 by Liu et al. and ex situ XRD diagnostics by Friedrich et al. further confirmed that the *c/a* ratio serves as a reliable and quantitative indicator of the lithium stoichiometry across different NMC compositions and cycling conditions [23, 24].

To keep consistency, the pouch cell's cathode was taken for characterization and methodology setup. Figure S1a–c shows that the NMC622 cathode is made of 10–15 μm secondary particles with a 1 μm primary particle, and the thickness is 51 μm. The EDS elemental mapping of C and O in Figure S1a shows that active material and conductive carbon are evenly distributed. Moreover, from the EDS spectra in Figure S1d, the sample mainly comprises Ni, Co, and Mn. The ratio among the elements is verified by EDS and ICP-MS, as shown in Table S1. The Ni/Co/Mn ratio from the quantification results matches the designed value. The crystalline structure was further verified by XRD, as shown in Figure S1e. The results indicate that the NMC622 material has a layered structure without other impurity phases. Figure S1f shows the first charge and discharge voltage profile of the NMC622 cathode. The charge capacity is 199.9 $mAh{\cdot}g^{-1}$ with an ICE of 85.8% for the voltage range of 3–4.3 V with a charge current of C/10. The areal loading is 3 $mAh{\cdot}cm^{-2}$.

In a layered structure cathode, the valence of transition metal M (Ni, Co, Mn)-ion changes progressively when Li ions are removed, as does the ionic radius: Ni^{2+} (ionic radius 0.69 Å) → Ni^{3+} (0.56 Å) → Ni^{4+} (0.48 Å); Co^{3+}(ionic radius 0.75 Å) → Co^{4+}(0.67 Å). As a result, the edge-sharing MO_6 slabs shrink along lattice *a*. Meanwhile, MO_6 slabs become positively charged and repel each other along the *c*-axis, resulting in an expansion along the lattice *c-axis*. The structural change is mostly reversible

16146840, 0, Downloaded from https://advanced.onlinelibrary.wiley.com/doi/10.1002/aenm.71028 by University Of Chicago Library, Wiley Online Library on [06/05/2026]. See the Terms and Conditions (https://onlinelibrary.wiley.com/terms-and-conditions) on Wiley Online Library for rules of use; OA articles are governed by the applicable Creative Commons License

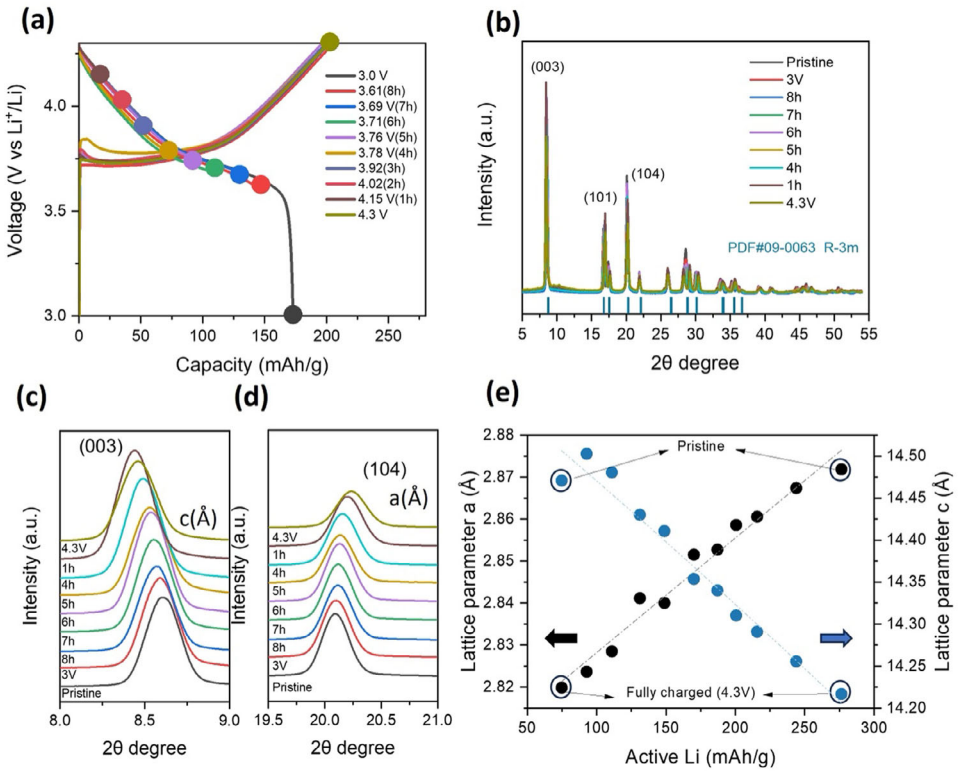

FIGURE 2 | (a) Voltage profile of NMC 622 half-cell with different quantities of Li inventory. (b) XRD spectra of the samples in (a) Amplification of the XRD spectra of (c) (003) peak and (d) (104) peak. (e) Relationship between lattice parameter a and lattice parameter c with active Li amount.

[25]. The reversible changes of lattice parameters *a* and *c*, along with the amount of Li, provide an avenue for quantifying the Li inventory of a layered cathode by XRD.

The Li inventory in the cathode after cycling can be divided into two parts. One is irreversible Li, which is consumed to form the Cathode-Electrolyte Interphase (CEI). The other one is active Li. The active Li comprises electrochemically active Li (discharge capacity) and residual Li within the cathode lattice. The theoretical capacity of NMC622 is 276.5 $mAh{\cdot}g^{-1}$, but the Li utilization (charge capacity) depends on the upper cut-off voltage. When charged to 4.3 V, it can deliver about 200 $mAh{\cdot}g^{-1}$ charge capacity as electrochemically active Li, and the remaining 76.5 $mAh{\cdot}g^{-1}$ Li will be in the cathode. The electrochemically active Li goes to the anode to provide capacity. The remaining Li is preserved as an additional Li source in the cathode and can be involved in the charge/discharge cycling if a higher voltage is applied.

To build the relationship between lattice parameters and the Li inventory, NMC622 cathodes with different Li inventories are prepared in the half cell by controlling the discharge cut-off voltage and time. The discharge state was chosen to avoid CEI formation interference because CEI growth is believed to only happen during the charging process. Therefore, the Li inventory change is only related to active Li in NMC622. Ten samples were prepared, including pristine, charged to 4.3 V, and then discharged to different depths of discharge by stopping at different discharge times, as shown in Figure 2a. The charge and discharge voltage profiles among the cells align well with a similar charge capacity. Table S2 shows the open circuit voltage (OCV) and corresponding charge and discharge capacity of the cells at different depths of discharge from Figure 2a. Here, the Li inventory (active Li) is calculated based on the theoretical capacity of NMC622, as shown in Equation 2. The calculated Li inventory is listed in Table S2 in a light green color.

$$\text{Li inventory (mAh/g)} = \text{Theorical (276.5mAh/g)} - \text{charge (mAh/g)} + \text{discharge (mAh/g)} \quad (2)$$

XRD was performed on the NMC622 cathode samples shown in Figure 2a, and the results are shown in Figure 2b–d. All of the samples retained a layered structure. When Li-ions are de-intercalated from the layer, the valence of Ni and Co ions changes progressively, with the ionic radius decreasing. As a result, the shrinkage happened along parameter *a*, which will cause the (104) peak position to shift right. Meanwhile, the expansion occurs along parameter *c*, which will cause (003) peak position to shift left. In Figure 2c, d, the zoom-in pictures of the (003) and (104) peaks show significant peak shifts with different amounts of Li.

We implemented XRD refinement to obtain the *a* and *c* values, which can be calculated based on Bragg's Law, as described in Note S1. Combining Li inventory capacity from Table S2, the calibration curve between lattice parameters and Li inventory amount was established, as shown in Figure 2e. The lattice parameters *a* show a linear relationship with active Li content, and lattice parameter *c* shows a quadratic relationship with the amount of active Li. Cell parameters *c* and *a* will change at the

16146840, 0, Downloaded from https://advanced.onlinelibrary.wiley.com/doi/10.1002/aenm.71028 by University Of Chicago Library, Wiley Online Library on [06/05/2026]. See the Terms and Conditions (https://onlinelibrary.wiley.com/terms-and-conditions) on Wiley Online Library for rules of use; OA articles are governed by the applicable Creative Commons License

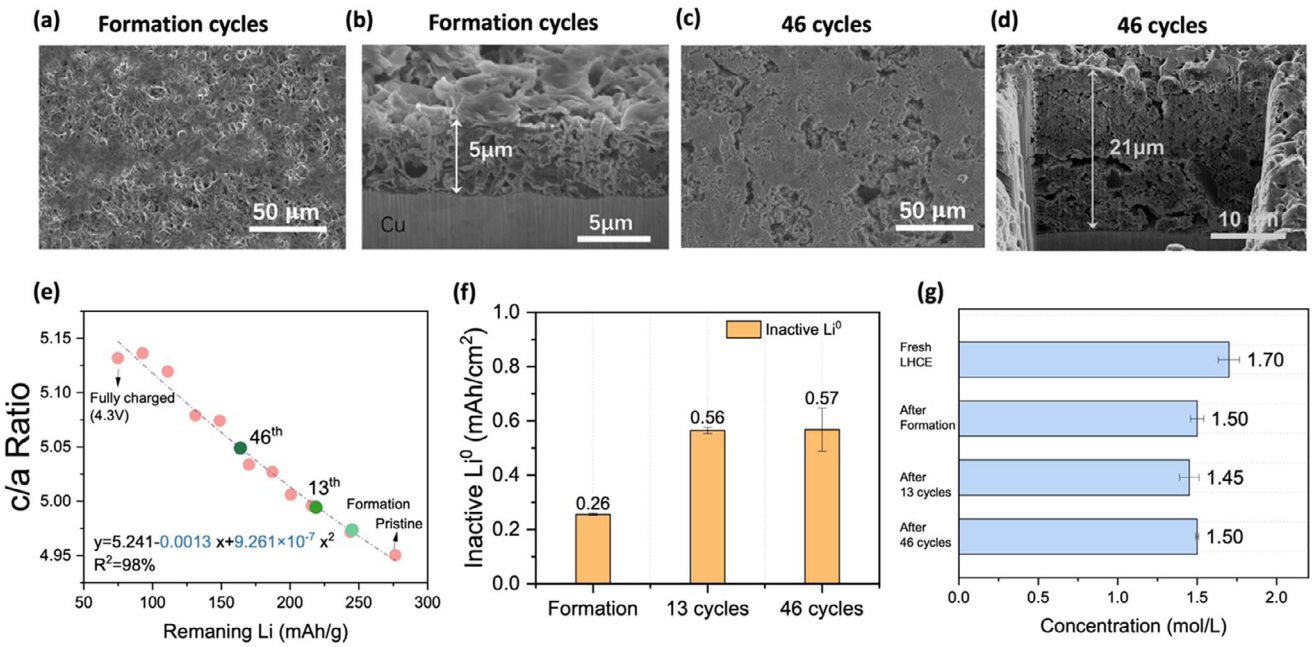

FIGURE 3 | SEM images of the surface and cross-section morphology of the cycled anode (a,b) after the formation cycle and (c,d) after 46 cycles. (e) Calibration curve for c/a ratio, active Li amount, and Li inventory in the cathode after different cycles. (f) TGC results on the cycled anode after different cycles. (g) Li concentration from the cycled electrolyte.

same time. Therefore, the value of the *c/a* ratio serves as the lattice parameter indicator for the NMC622 cathode. The calibration curve is shown in Figure 3e. By this method, XRD on a cycled NMC622 cathode helps to confirm the Li inventory. It is worth noting that the calibration curve in Figure 3e is accurate only if the structure of the NMC622 cathode is stable upon cycling. The detailed verification process is listed in Figure S2, Table S3, and Note S2.

2.3 | Li Inventory Quantification in NMC622-Anode Free (No Excessive Li Reservoir) Cells

After the cells underwent formation cycles, 13 cycles, and 46 cycles, we disassembled the cells, and the global morphology was investigated. Figure S3 shows the optical image of the anode, separator, and cathode. In a pristine state, a shiny and flat Cu current collector was present on the anode side. After the formation cycle, black deposits appeared on the anode, which further accumulated after 13 cycles. By 46 cycles, severe delamination of these black deposits was observed. The severe delamination of the black deposits implies the formation of the fluffy dead Li. However, no significant changes were observed on the cathode side, which implies the degradation of the cell is dominated by the anode. The surface and cross-section morphology of the cycled anode was further investigated by SEM, as shown in Figure 3a–d and Figure S4. The bare Cu exhibited a flat surface in the pristine state. After formation cycling, the anode shows a porous structure due to the accumulation of SEI growth. This high porosity and tortuosity morphology can induce a loss in the electronic pathway, resulting in active Li^0 being trapped within the SEI and becoming inactive, as shown in Figure S5. Besides, it also induces Li to grow with whisker-like morphology, which will consume the electrolyte due to the high surface area, as shown in the cross-sectional morphology. The thickness of the dead Li after 46 cycles is 4 times thicker than the formation sample.

The formation of the dead Li on the anode consists of inactive Li^0 and SEI Li, in which the Li in SEI is not only from the cathode but also from the electrolyte. As shown in Equation 1, cathode Li inventory quantification is required to quantify the total SEI amount. With the developed methodology, Figure S6 shows the XRD results of the cycled cathode. The cathode structure was observed to have been preserved well in both electrolytes. From the Li inventory quantification results in Figure 3e and Table S4, the value of the *c/a* ratio increased with cycling, indicating active Li loss from the cathode. The residual Li within the cathode lattice decreases, indicating it serves as a Li reservoir in the cathode. To quantify the trapped Li^0 in the anode, we performed the TGC on the punched anode with separators to ensure that all substances participate in the titration reaction. The results are shown in Figure 3f. It shows that the amount of trapped inactive Li^0 increases during the initial cycles, and no further increase is observed in the following cycles. The formation of the SEI may consume Li from the cathode and salt in the electrolyte. In advanced electrolytes such as LHCE [26] and in dual salt electrolytes [27], the salts' decomposition facilitates the formation of stable SEI, resulting in stable cycling. The electrolyte depletion also affects cycling stability. Therefore, the Li inventory quantification study should also consider Li inventory in the electrolyte. Figure S7a,b show the process for the electrolyte collection. With lean electrolytes, it is hard to collect fluid electrolytes from the cycled pouch cell since the electrolyte is trapped in the pores of the electrodes. Here, we applied a centrifuge process for the cycled pouch cells to collect the electrolyte. We cut open the cycled pouch cell and placed it in the centrifuge tube, then centrifuged the sample at the rate of

16146840, 0, Downloaded from https://advanced.onlinelibrary.wiley.com/doi/10.1002/aenm.71028 by University Of Chicago Library, Wiley Online Library on [06/05/2026]. See the Terms and Conditions (https://onlinelibrary.wiley.com/terms-and-conditions) on Wiley Online Library for rules of use; OA articles are governed by the applicable Creative Commons License

2500 rpm for 10 mins at room temperature (RT). The electrolyte is collected at the bottom of the tube. Since the centrifuge process is conducted outside the glovebox, we examined the air tightness of the tube with a commercial fresh Li metal chip to verify possible sample contamination during the electrolyte collection. The Li chip showed the same shiny surface as the Li chip in the glove box, indicating that the sample would not be contaminated by this step. After collecting the electrolyte, an ICP-MS measurement was performed to quantify the Li^+ concentration in the electrolyte for the cells that underwent different numbers of cycles, as shown in Figure 3g. After the formation cycle, the Li^+ concentration decreased from 1.7 to 1.5 M. Upon cycling, no significant Li^+ concentration changes were observed. However, from SEM images of the cross-section, it was observed that the thickness of dead Li increases upon cycling, indicating that the salts and solvent decompose simultaneously. The NMR test was performed on the LHCE electrolyte after different cycles. $CDCL_3$ was applied to dilute the collected electrolyte. All the cycled electrolytes show similar signals to the pristine one, and no new peaks are observed in ^1H and ^{13}C NMR spectra, as shown in Figure S8. The results imply that the electrolyte decomposition would not produce soluble species, while the by-product mainly accumulated on the anode, as shown in Figure S3 and Figure 3.

The TEM and XPS further revealed the interphase information on the anode and cathode. Figure 4a–c show the morphology and structure of the cathode interphase. No coating layer is observed on the pristine sample. After the formation cycle, as shown in Figure 4b, a thin CEI layer with a thickness of 6.5 nm is observed on the cathode surface. After 46 cycles, the thickness of CEI is increased to 10 nm average from the TEM results, as shown in Figure 4c. To estimate the amount of CEI Li, we assume that the entirety of the CEI consists of LiF, and by estimating the surface area, the consumption of Li in the CEI is less than 1% after 46 cycles, as indicated in Figure S9 and Note S3. However, a notable difference is observed in the anode interphase. After the formation cycle, XPS F 1s and Li 1s spectra show that the dominant inorganic SEI components are LiF and Li_2O, as shown in Figure 4d. After 46 cycles, Li_2O disappeared, and more LiF was detected. The increased intensity of organic species detected in C 1s and O1s indicates the decomposition of the solvent. XPS depth profiling was further applied to understand the distribution of elements in SEI portraits. As shown in Figure 4e, g, quantitative XPS analysis reveals that the F atomic ratio in the SEI increases 6.3-fold from formation (1.5%) to 46 cycles (9.5%), uniformly across all sputtering depths, while C and O increase more modestly (C 10.5% to 24% and O 25.5% → 27.5% respectively), demonstrating that LiFSI salt anion decomposition becomes the dominant SEI-forming mechanism in Stage III, accompanied by a slower but concurrent contribution from solvent decomposition. Considering the negligible amount of CEI, the results further verified that electrolyte depletion happened mainly on the anode surface.

Figure 5a summarizes Li inventory changes in the NMC622-anode free pouch cell. The Li inventory in the electrolyte is calculated based on the injection amount (600 uL). The Li decrement in the cathode and electrolyte equals the increment of SEI and trapped Li^0 on the anode side. In the pristine state, 363.6 mAh of Li was in the cathode, and 27.3 mAh was in the electrolyte. After formation, the cathode lost 41.7 mAh of Li, and the electrolyte consumed 3.2 mAh of Li. These Li losses were gained by the anode in the form of SEI (13.3mAh) and inactive Li^0 (22.8 mAh). After 46 cycles, the cathode lost 146.4 mAh of Li, and the electrolyte consumed >3.2 mAh of Li. Most have formed SEI on the anode. Therefore, the black substance on the anode side observed in Figure S3 after 46 cycles comprised >99.2 mAh of SEI and 49.9 mAh of inactive Li^0. The increase in the SEI will build up cell impedance as well. The impedance change upon cycling in the NMC622-anode free pouch cells is shown in Figure 5a. Here, R_s is related to the cell's impedance, including the electrolyte, case, current collector, etc. No significant changes are observed in the R_s value upon cycling. R_{ct} is charge transfer impedance related to the cell's interphase impedance. The cell shows charge transfer impedance increments from 1.5 to 3.5 Ω after 13 cycles and further increases to 10 Ω after 46 cycles. The results are consistent with the cross-section images that thick dead Li results in impedance increases.

3 | Discussion

Integrating all component-resolved Li-inventory measurements and electrochemical analyses, we identify a three-stage evolution pathway that governs performance, energy density, and safety in anode-free NMC622||Cu cells, as shown in Figure 6. In Stage I (formation), approximately 41.7 mAh of Li (11.5% of the cathode's initial inventory) is irreversibly transferred from the cathode to the Cu current collector. This Li is partitioned into SEI Li (13.3 mAh), inactive Li^0 (22.8 mAh), and a small electronically connected reservoir of active plated Li. Loss of Li in the electrolyte remains comparatively small (3.2 mAh, 11.7% of the electrolyte Li), and CEI formation on NMC622 accounts for <1% of total Li consumption, as detailed in Table S5. This confirms that CEI formation contributes negligibly to early Li loss compared to anode interphase formation. Because anode-free cells do not contain an excess Li reservoir, each milliampere-hour of Li consumed during formation directly reduces the usable active Li from the cathode and thereby lowers the practical energy density prior to cycling. These results demonstrate that Li depletion on the cathode side and not electrolyte decomposition is the dominant irreversible process in Stage I and highlight the importance of preserving the initial Li inventory through cathode pre-lithiation, lithium-rich formulations, and sacrificial-Li additives, as well as early interphase stabilization via current collector pretreatment.

Stage II (midlife cycling) is governed by the continued accumulation of inactive Li^0. SEM images confirm the increased tortuosity and the emergence of whisker-like morphologies, which promote electronic disconnection and thereby accelerate the formation of inactive Li^0. Inactive Li^0 nearly doubles (22.8 → 49.1 mAh), emerging as the primary irreversible Li sink. In contrast, SEI Li remains essentially unchanged (~13.3 mAh), indicating that interphase thickening is not yet the dominant degradation mode. During this stage, the cathode's residual lattice Li begins to provide limited compensation (~15 mAh), temporarily sustaining coulombic balance and masking internal degradation. This stage defines the effective cycle life window: although external metrics (capacity, CE, and voltage profiles) remain stable, the internal loss of electronic connectivity at the anode progresses. From a design perspective, Stage II highlights that controlling Li plating morphology, minimizing electronic

16146840, 0, Downloaded from https://advanced.onlinelibrary.wiley.com/doi/10.1002/aenm.71028 by University Of Chicago Library, Wiley Online Library on [06/05/2026]. See the Terms and Conditions (https://onlinelibrary.wiley.com/terms-and-conditions) on Wiley Online Library for rules of use; OA articles are governed by the applicable Creative Commons License

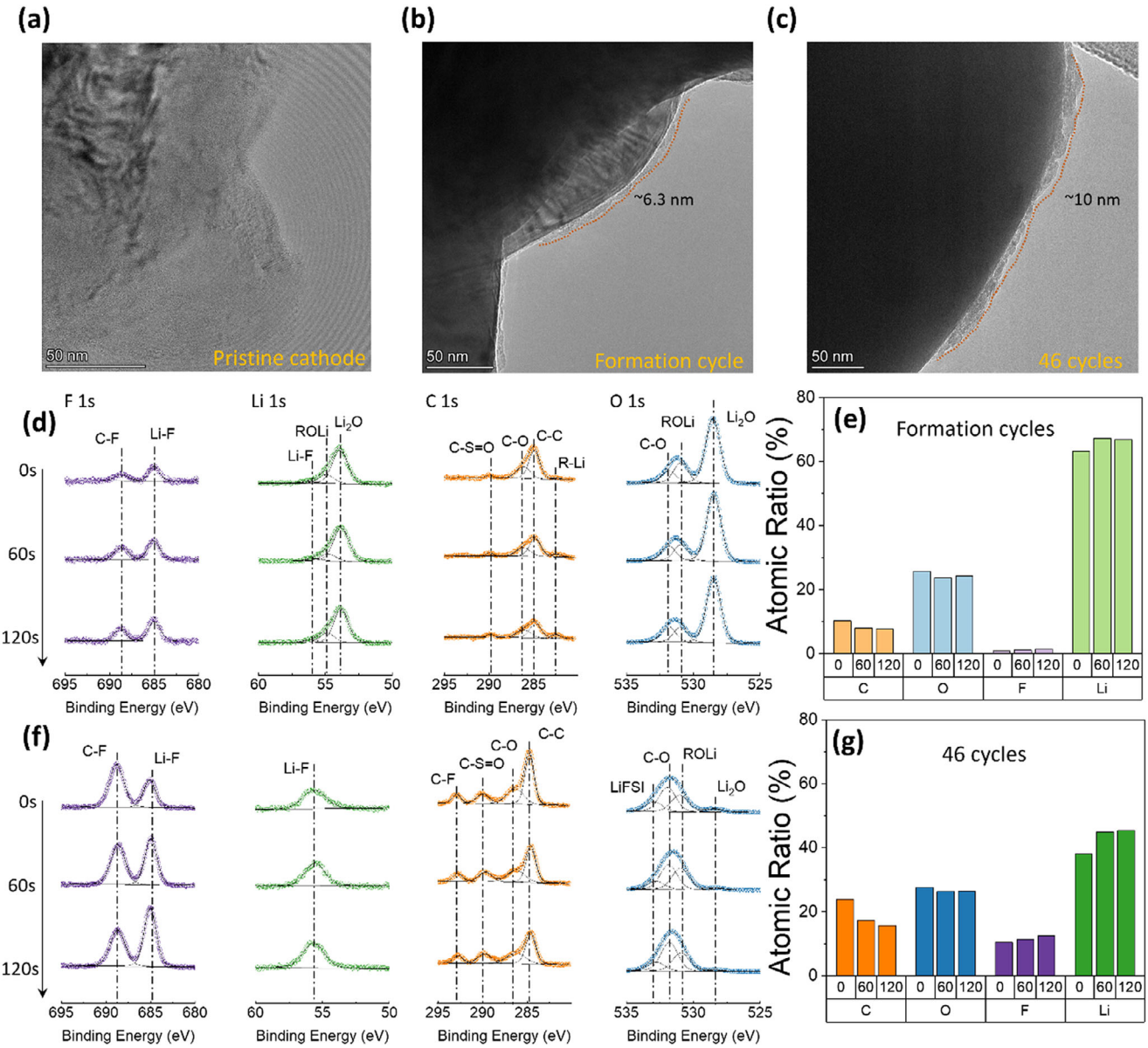

FIGURE 4 | HRTEM images of NMC622 cathode interphase at (a) pristine state, (b) after formation, and (c) 46 cycles. (d) XPS spectra and atomic ratio of C, O, F, and Li on cycled anode from XPS depth profile after (d, e) formation cycle and (f, g) 46 cycles.

isolation, and maintaining conductive pathways are more critical than suppressing SEI growth at this stage. Recent molecular interphase engineering strategies — including 2D polyamide and DNA interphase layers—have demonstrated the ability to homogenize Li^+ flux and optimize SEI composition, thereby mitigating inactive Li^0 accumulation at the anode side [28, 29].

Stage III (higher number of cycles) The transition from Stage II to Stage III is quantitatively identified by a shift in the dominant Li loss mechanism: SEI Li growth accelerates sharply (30.7 → 99.2 mAh, +223%), surpassing inactive Li^0 as the primary Li sink, accompanied by a pronounced rise in charge-transfer resistance (~3.5 → ~10 Ω), together marking the onset of the safety-critical regime. 1H/13C NMR shows no new soluble products, implying decomposition products largely accumulate at the anode (consistent with cross-section SEM). This extensive interphase growth drives over a five-fold rise in charge-transfer resistance and produces strong interphase heterogeneity, leading to non-uniform Li deposition, localized heating, and increasing thermal gradients. These heterogeneities elevate local current densities and may create hotspots, raising safety concerns in later-stage cycling. At the same time, the cathode continues to lose Li, with a growing fraction of its residual lattice Li being released to compensate for anode-side inefficiencies. Although this compensatory mechanism temporarily sustains capacity, it diminishes over time as structural changes in the NMC particles limit the accessibility of residual Li. Together, the interplay between runaway SEI formation and the progressive reliance on cathode lattice Li marks Stage III as the region where the most degradation occurs and is the safety-critical regime. These results highlight the need for electrolytes that inhibit aggressive SEI growth, and provide mechanically robust interphases and cathode-stabilization strategies that moderate residual-Li release during extended cycling.

16146840, 0, Downloaded from https://advanced.onlinelibrary.wiley.com/doi/10.1002/aenm.71028 by University Of Chicago Library, Wiley Online Library on [06/05/2026]. See the Terms and Conditions (https://onlinelibrary.wiley.com/terms-and-conditions) on Wiley Online Library for rules of use; OA articles are governed by the applicable Creative Commons License

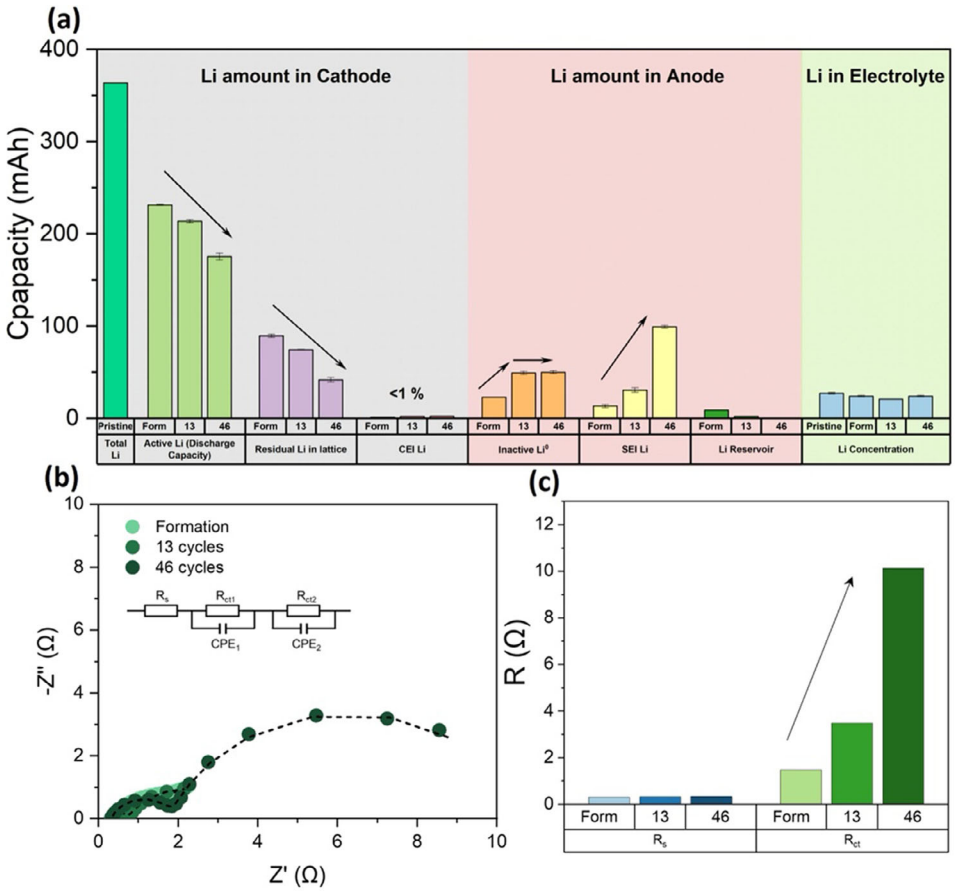

FIGURE 5 | (a) NMC 622-anode free pouch cell Li inventory changes upon cycling in LHCE electrolyte. (b) Cell impedance change upon cycling with and (c) Charge transfer impedance value from (b). Rs is the intrinsic cell impedance. Rct is charge transfer impedance. The value is the sum of Rct_1 and Rct_2.

When comparing anode-free batteries with conventional Li-metal and Li-ion batteries, capacity degradation in all three systems is ultimately linked to SEI buildup; however, the degradation pathways and the sources of consumed lithium differ fundamentally. In Li-ion batteries, lithium loss is dominated by SEI-related Li^+ consumption driven by electrode crosstalk, with lithium inventory depletion originating primarily from electrochemically cyclable lithium in the cathode. Accordingly, suppressing cross-talk through cathode surface coatings (e.g., Al_2O_3) and boron-based electrolyte additives can effectively extend cycle life [9]. In Li-metal batteries with excess lithium, continued formation of inactive metallic Li^0 contributes to sustained SEI growth, introducing nonlinear and less predictable degradation behavior dominated by depletion of the anode lithium reservoir. As a result, SEI stabilization and electrolyte development emerge as primary performance levers [30]. In contrast, anode-free batteries lack an intrinsic lithium reservoir, forcing lithium depletion from both the electrolyte and the cathode, including electrochemically cyclable lithium and residual lattice lithium. Loss of the latter is strongly coupled to cathode structural instability and kinetic limitations under extreme delithiation, thereby accelerating failure and increasing safety risks. Consequently, performance improvement in anode-free batteries is inherently more challenging and requires a system-level strategy that extends beyond electrolyte and SEI optimization to include cathode designs with high structural stability and lithium-buffering capability, such as lithium-rich or sacrificial-lithium cathodes.

4 | Conclusion

In summary, this work establishes a quantitative, component-resolved framework for tracking Li inventory in anode-free NMC622||Cu cells by integrating XRD-based cathode analysis, TGC quantification of inactive Li^0, and electrolyte/interphase characterization. This approach enables clear differentiation between reversible cathode Li, residual lattice Li, inactive metallic Li, and SEI Li, allowing the full Li balance of the cell to be resolved across cycling. The results reveal a sequential transition in the dominant irreversible Li-loss pathways: early formation-driven cathode Li depletion, midlife inactive Li accumulation, and late-stage SEI thickening accompanied by rising impedance and exhaustion of the residual lattice Li reservoir. By quantitatively resolving where Li resides, how it evolves, and when it is irreversibly consumed, this framework identifies cathode optimization as a governing factor for anode-free battery performance. In the absence of an intrinsic lithium reservoir, the cathode acts as the sole lithium source throughout cycling, making cathode structural stability, lattice-Li accessibility, and lithium-buffering capability decisive in controlling cycle life, energy density, and safety. Accordingly, cathode designs that

16146840, 0, Downloaded from https://advanced.onlinelibrary.wiley.com/doi/10.1002/aenm.71028 by University Of Chicago Library, Wiley Online Library on [06/05/2026]. See the Terms and Conditions (https://onlinelibrary.wiley.com/terms-and-conditions) on Wiley Online Library for rules of use; OA articles are governed by the applicable Creative Commons License

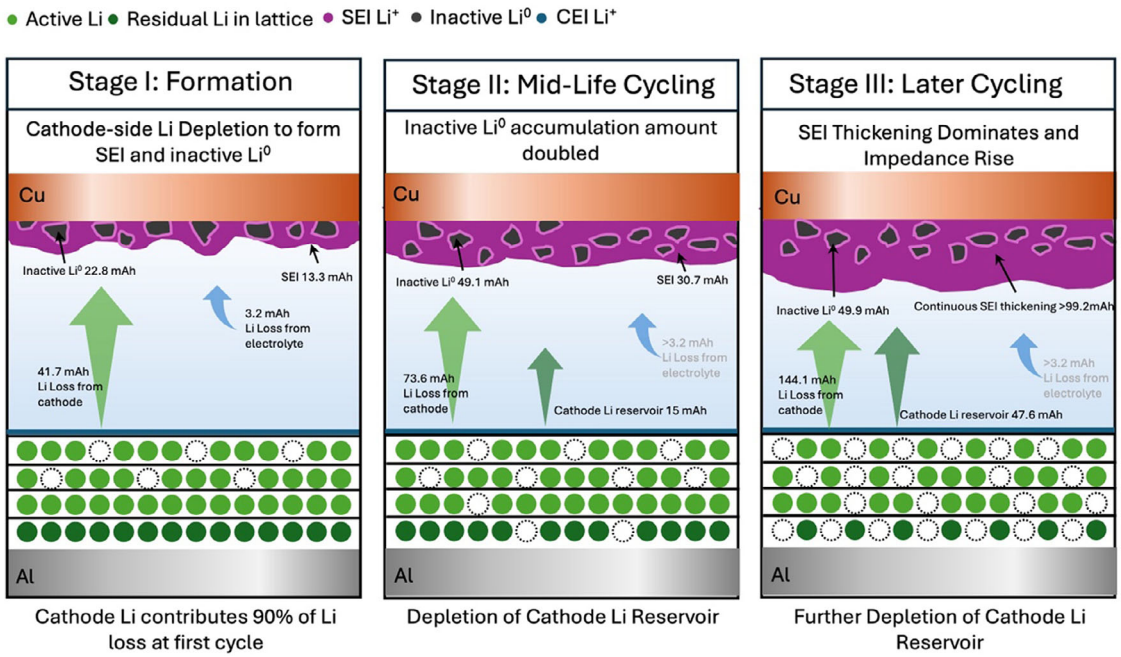

FIGURE 6 | Schematic illustration of Li inventory evolution in anode-free NMC622||Cu pouch cells across three characteristic stages. Stage I (formation) is dominated by initial SEI growth and inactive Li^0 accumulation, driven primarily by Li consumption from the cathode. Stage II (mid-cycle) shows continued growth of inactive Li^0 as the major irreversible Li loss, while the cathode lattice Li reservoir begins to supplement anode-side losses. In Stage III (later cycle), extensive SEI thickening (>99.2 mAh equivalent Li) and progressive depletion of the cathode lattice Li reservoir accelerate overall Li inventory loss, elevate interfacial impedance, and ultimately trigger rapid capacity fade.

preserve structural integrity under extreme delithiation and enable controlled utilization of residual lattice Li—through lithium-rich or sacrificial-lithium strategies—are essential to delay irreversible inventory exhaustion. More broadly, the methodology and stage-resolved dataset developed here provide a quantitative foundation for accelerating the development of safe, high-energy, and long-life anode-free lithium metal batteries.

5 | Experimental Section

5.1 | Electrochemical Tests

5.1.1 | Half Cell

The NMC622 electrode (3 mAh/cm^2) from dry pouch cells (Li-Fun Technology Inc.) with a diameter of 3/8 inches as the working electrode was assembled into a 2032 type coin cell in an Ar-filled glove box. Li metal (1 mm thick, 0.5 inches in diameter) was employed as the counter electrode. The electrolyte amount was fixed at 75 uL per cell. The half cell was cycled between 3 V and 4.3 V at room temperature at a current density of C/10 during the first cycle and C/3 for subsequent cycles, using a Neware battery tester. We controlled the discharge to different depths for the XRD test by limiting the cut-off voltage and time of discharge.

5.1.2 | Pouch Cell

Commercial NMC622- anode-free dry pouch cells from Li-Fun Technology Inc. were utilized for methodology development. All pouch cells were sealed in an Ar-filled glove box after electrolyte injection. The electrolyte amount was 600 µL. The cells were kept in a pressure fixture with a stacking pressure of 350 kPa. The pouch cell was cycled between 3 and 4.3 V at room temperature at a current density of C/10 during the first two formation cycles and C/3 for subsequent cycles, using an Arbin battery tester.

5.2 | Characterizations

5.2.1 | Electrochemical Impedance Spectroscopy (EIS)

Characterization of potentiostatic electrochemical impedance (EIS) was performed using a BioLogic SP-150 workstation under OCV at 0% SOC with the 1 MHz -10 mHz as the frequency range, with 5 mV RMS. A symmetric coin cell was assembled using the cycled anode at 0% SOC. One side of the anode surface was gently scraped using a blade, and two 1/4-inch electrode disks were punched. A Celgard 2325 separator and 50 µL of LHCE electrolyte were used to assemble the cell for evaluating the interphase impedance evolution. The SEI impedance was determined as the sum of R_ct1 and R_ct2 obtained from the equivalent circuit fitting; the fitting accuracy is 99%.

5.2.2 | Cryogenic Focused Ion Beam-Scanning Electron Microscopes

The Cryo FIB-SEM was conducted with the FEI Scios Dual-beam microscopy. The samples were transferred to the FIB chamber without exposure to air. The electron beam operating voltage was 5 kV, and the stage was cooled with liquid nitrogen to −180°C. Sample cross-sections were exposed using a 30 nA ion beam current and cleaned at 0.3 nA.

16146840, 0, Downloaded from https://advanced.onlinelibrary.wiley.com/doi/10.1002/aenm.71028 by University Of Chicago Library, Wiley Online Library on [06/05/2026]. See the Terms and Conditions (https://onlinelibrary.wiley.com/terms-and-conditions) on Wiley Online Library for rules of use; OA articles are governed by the applicable Creative Commons License

5.2.3 | Capillary X-Ray Diffraction Measurements

The samples were prepared by sealing the powders into 0.5 mm-diameter boron-rich glass capillaries (Charles Supper) in an Ar-filled glovebox. XRD patterns were obtained with a Bruker Apex II Ultra diffractometer with Mo Kα radiation (λ = 0.70932 Å) at 50 kV and 50 mA over a 2θ range of 5–40°.

5.2.4 | Titration-Gas Chromatography (TGC)

The TGC experiments were performed using a Shimadzu GC-2010 Plus Tracera equipped with a barrier ionization discharge (BID) detector. The Split temperature was kept at 200°C with a split ratio of 2.5 (split vent flow: 20.58 mL·min^{-1}, column gas flow: 8.22 mL·min^{-1}, purge flow: 0.5 mL·min^{-1}). Column temperature (RT-Msieve 5A, 0.53 mm) was kept at 40°C, and the BID detector was held at 235°C. Helium (99.9999%) was used as the carrier gas, and the BID detector gas flow rate was 50 mL·min^{-1}. The electrode sample was put in a septum-sealed glass vial, and after injecting the 0.5 mL ethanol (200 proof anhydrous), the sample gases were injected into the machine via a 50 µL gas-tight Hamilton syringe.

5.2.5 | Inductively Coupled Plasma—Mass Spectrometry (ICP-MS)

The collected electrolyte was diluted with ICP matrix solution (0.5% HCl + 0.5% HNO_3 in H_2O) to form 10 mL of ICP sample. ICP-MS was performed with a Thermo iCAP RQ ICP-MS to analyze the Li concentration in pristine and cycled electrolytes.

5.2.6 | Nuclear Magnetic Resonance (NMR)

NMR was conducted on electrolytes to analyze the salt species in the electrolyte. The NMR measurements of the electrolyte samples were performed with a JEOL ECA 500 spectrometer. For the LHCE electrolyte, $CDCl_3$ solvent was utilized, and anhydrous deuterated dimethyl sulfoxide (d-DMSO) was applied to form a clear solution. The NMR sample was then sealed in an NMR tube inside the Ar-filled glovebox for further measurement. The NMR spectra were analyzed with MestReNova.

5.2.7 | X-Ray Photoelectron Spectroscopy (XPS)

The XPS was conducted on Kratos AXIS-Supra, using an Al target as the X-ray source under 10^{-9} Torr pressure. The cycled electrodes for XPS tests were rinsed with DMC and then transferred to the nitrogen-filled glovebox directly connected to the chamber without air exposure. Survey scans were performed with a step size of 1.0 eV, followed by a fine scan with 0.1 eV resolution. The spectra were analyzed by CasaXPS software to identify the different chemical species.

5.2.8 | Transmission Electron Microscopy (TEM)

The cycled samples were transferred to a TEM (ThermoFisher Talos 200X TEM operated at 200 kV) using an airtight transfer method. STEM-based energy-dispersive X-ray spectroscopy (STEM-EDS) was performed on a ThermoFisher Talos 200X TEM with 4 in-column SDD Super-X detectors operated at 200 kV. The probe current for EDS maps on the TALOS was 140 pA with an acquisition time of 3 min in total. EDS mapping was acquired from areas with low-dose technology to minimize possible electron beam irradiation effects. The ThermoFisher Talos 200X TEM electron microscope system was fitted with a Schottky X-ray FEG field emission electron gun, STEM model. The SAED (selected area electron diffraction) images are acquired with an electron dose rate ~0.1 e Å^{-2} s^{-1} for 4s (FEI Ceta camera).

The pristine sample was checked with ThermoFisher Scientific Iliad UItra scanning transmission electron microscope, a next-generation sub-angstrom analytical electron optical beam line with a 30–300 kV coherent, ultra-monochromated probe FEG corrected source. TEM experiments were executed on a Falcon IVi direct electron detector with the conditions of 300 kV, 100pA, and a probe diameter of 270 nm for a dose rate of 110 eÅ^{-2}s^{-1}.

Cryo-TEM and STEM were conducted with Thermo Fisher Scientific Spectra Ultra X (Iliad) scanning transmission electron microscope operated at 300 k and −170 C with a Simple Origin Model 201 inert gas transfer cryogenic TEM holder.

Author Contributions

W.B., and Y.S.M. conceived the ideas. W.B. prepared electrodes and cycled the cells. W.B. fabricated the half-cell, conducted electrochemical cycling, and did TGC measurement. W.B. wrote the manuscript. W.B. and A.L. conduct SEM. T.S.M. and Y.B.Z. performed TEM experiments. W.B. and W.L. designed and conducted XPS experiments, and W.L. performed XRD refinement. All authors discussed the results and commented on the manuscript.

Acknowledgements

The authors gratefully acknowledge funding supported by the Underwriters Laboratories Research Institutes. TEM, SEM and Cryo-FIB-SEM were performed at the San Diego Nanotechnology Infrastructure (SDNI) of UCSD, a member of the National Nanotechnology Coordinated Infrastructure supported by the National Science Foundation (Grant ECCS-1542148). The authors acknowledge the use of facilities and instrumentation at the UC Irvine Materials Research Institute (IMRI), which is supported in part by the National Science Foundation through the UC Irvine Materials Research Science and Engineering Center (DMR-2011967). Specifically, the XPS work was performed using instrumentation funded in part by the National Science Foundation Major Research Instrumentation Program under Grant Number. CHE-1338173. The ThermoFisher Scientific Iliad Ultra Scanning Transmission Electron Microscope was developed as part of a CRADA #01300710 between Argonne National Laboratory and ThermoFisher Scientific Instruments. The authors also acknowledge the use of facilities and instrumentation supported by NSF through the UC San Diego Materials Research Science and Engineering Center (UCSD MRSEC), DMR-2011924. The authors acknowledge Neware Instruments for the battery test system donation. The authors acknowledge Yixuan Li for assistance with NMR measurements, Bing Han for TEM measurements, Baharak Sayahpour for XRD measurements, and Ryosuke Shimizu for ICP-MS measurements. The authors acknowledge the support from Dr. Sateesh Madhi from UL Research Institutes on the management of the project requirements.

Conflicts of Interest

The authors declare no conflict of interest.

16146840, 0, Downloaded from https://advanced.onlinelibrary.wiley.com/doi/10.1002/aenm.71028 by University Of Chicago Library, Wiley Online Library on [06/05/2026]. See the Terms and Conditions (https://onlinelibrary.wiley.com/terms-and-conditions) on Wiley Online Library for rules of use; OA articles are governed by the applicable Creative Commons License

Data Availability Statement

The data that support the findings of this study are available from the corresponding author upon reasonable request.

References

1. A. Yoshino, "The Birth of the Lithium-Ion Battery," *Angewandte Chemie International Edition* 51, no. 24 (2012): 5798–5800, https://doi.org/10.1002/anie.201105006.

2. L. Chen, X. Fan, X. Ji, J. Chen, S. Hou, and C. Wang, "High-Energy Li Metal Battery With Lithiated Host," *Joule* 3, no. 3 (2019): 732–744, https://doi.org/10.1016/j.joule.2018.11.025.

3. J. Qian, W. A. Henderson, and W. Xu, "High Rate and Stable Cycling of Lithium Metal Anode," *Nature communications* 6, no. 1 (2015): 6362, https://doi.org/10.1038/ncomms7362.

4. S. Nanda, A. Gupta, and A. Manthiram, "Anode-Free Full Cells: A Pathway to High-Energy Density Lithium-Metal Batteries," *Advanced Energy Materials* 11, no. 2 (2021): 2000804, https://doi.org/10.1002/aenm.202000804.

5. A. Louli, A. Eldesoky, and R. Weber, "Diagnosing and Correcting Anode-free Cell Failure via Electrolyte and Morphological Analysis," *Nature Energy* 5, no. 9 (2020): 693–702, https://doi.org/10.1038/s41560-020-0668-8.

6. D.-H. Liu, Z. Bai, and M. Li, "Developing High Safety Li-metal Anodes for Future High-energy Li-metal Batteries: Strategies and Perspectives," *Chemical Society Reviews* 49, no. 15 (2020): 5407–5445, https://doi.org/10.1039/C9CS00636B.

7. L. Wichmann, S.-K. Jiang, and J. H. Thienenkamp, "Origins of Lithium Inventory Reversibility With an Alloying Functional Layer in Anode-free Lithium Metal Batteries," *Nature Communications* 16, no. 1 (2025): 7216, https://doi.org/10.1038/s41467-025-62289-6.

8. S. Menkin, C. A. O'Keefe, and A. B. Gunnarsdóttir, "Toward an Understanding of SEI Formation and Lithium Plating on Copper in Anode-free Batteries," *The Journal of Physical Chemistry C* 125, no. 30 (2021): 16719–16732, https://doi.org/10.1021/acs.jpcc.1c03877.

9. W. Bao, W. Yao, and Y. Li, "Insights Into lithium inventory quantification of LiNi 0.5 Mn 1.5 O_4 –graphite full cells," *Energy & Environmental Science* 17, no. 12 (2024): 4263–4272, https://doi.org/10.1039/D4EE00842A.

10. J. Wang, Y. Zhou, and Y. Zhuo, "The Challenges and Strategies towards High-Performance Anode-Free Post-Lithium Metal Batteries," *Chemical Science* 16 (2025): 552–574.

11. C. Fang, J. Li, and M. Zhang, "Quantifying Inactive Lithium in Lithium Metal Batteries," *Nature* 572, no. 7770 (2019): 511–515, https://doi.org/10.1038/s41586-019-1481-z.

12. W. Zhu, H. Demers, and G. Girard, "Monitoring Lithium Metal Plating/Stripping in Anode Free//NMC811 Battery by In-Situ X-Rays Diffraction," *Journal of Power Sources* 546 (2022): 231941, https://doi.org/10.1016/j.jpowsour.2022.231941.

13. F. Geng, Q. Yang, C. Li, M. Shen, Q. Chen, and B. Hu, "Mapping the Distribution and the Microstructural Dimensions of Metallic Lithium Deposits in an Anode-free Battery by in Situ EPR Imaging," *Chemistry of Materials* 33, no. 21 (2021): 8223–8234, https://doi.org/10.1021/acs.chemmater.1c02323.

14. A. B. Gunnarsdóttir, C. V. Amanchukwu, S. Menkin, and C. P. Grey, "Noninvasive in Situ NMR Study of "Dead Lithium" Formation and Lithium Corrosion in Full-cell Lithium Metal Batteries," *Journal of the American Chemical Society* 142, no. 49 (2020): 20814–20827, https://doi.org/10.1021/jacs.0c10258.

15. J. Betz, J. P. Brinkmann, and R. Nölle, "Cross Talk Between Transition Metal Cathode and Li Metal Anode: Unraveling Its Influence on the Deposition/Dissolution Behavior and Morphology of Lithium," *Advanced energy materials* 9, no. 21 (2019): 1900574, https://doi.org/10.1002/aenm.201900574.

16. C.-J. Huang, B. Thirumalraj, and H.-C. Tao, "Decoupling the Origins of Irreversible Coulombic Efficiency in Anode-free Lithium Metal Batteries," *Nature Communications* 12, no. 1 (2021): 1452, https://doi.org/10.1038/s41467-021-21683-6.

17. M. Li, Y. Zhang, H. Zhou, F. Xin, M. S. Whittingham, and B. Liaw, "Lithium Inventory Tracking as a Non-destructive Battery Evaluation and Monitoring Method," *Nature Energy* 9 (2024): 1–10.

18. C. Gervillie-Mouravieff, L. Ah, A. Liu, C.-J. Huang, and Y. S. Meng, "Deciphering the Impact of the Active Lithium Reservoir in Anode-free Pouch Cells," *ACS Energy Letters* 9, no. 4 (2024): 1693–1700, https://doi.org/10.1021/acsenergylett.4c00457.

19. A. Louli, M. Coon, M. Genovese, J. deGooyer, A. Eldesoky, and J. Dahn, "Optimizing Cycling Conditions for Anode-free Lithium Metal Cells," *Journal of the Electrochemical Society* 168, no. 2 (2021): 020515, https://doi.org/10.1149/1945-7111/abe089.

20. C. Gervillié-Mouravieff, L. Ah, A. Liu, C.-J. Huang, and Y. S. Meng, "Deciphering the Impact of the Active Lithium Reservoir in Anode-free Pouch Cells," *ACS Energy Letters* 9, no. 4 (2024): 1693–1700, https://doi.org/10.1021/acsenergylett.4c00457.

21. W. Deng, X. Yin, and W. Bao, "Quantification of Reversible and Irreversible Lithium in Practical Lithium-metal Batteries," *Nature Energy* 7, no. 11 (2022): 1031–1041, https://doi.org/10.1038/s41560-022-01120-8.

22. X.-L. Wang, K. An, and L. Cai, "Visualizing the Chemistry and Structure Dynamics in Lithium-ion Batteries by in-situ Neutron Diffraction," *Scientific Reports* 2, no. 1 (2012): 747, https://doi.org/10.1038/srep00747.

23. F. Friedrich, B. Strehle, and A. T. Freiberg, "Editors' Choice—Capacity Fading Mechanisms of NCM-811 Cathodes in Lithium-Ion Batteries Studied by X-ray Diffraction and Other Diagnostics," *Journal of The Electrochemical Society* 166, no. 15 (2019): A3760–A3774, https://doi.org/10.1149/2.0821915jes.

24. C. D. Quilty, D. C. Bock, S. Yan, K. J. Takeuchi, E. S. Takeuchi, and A. C. Marschilok, "Probing Sources of Capacity Fade in LiNi0. 6Mn0. 2Co0. $2O_2$ (NMC622): An Operando XRD Study of Li/NMC622 Batteries During Extended Cycling," *The Journal of Physical Chemistry C* 124, no. 15 (2020): 8119–8128, https://doi.org/10.1021/acs.jpcc.0c00262.

25. X.-L. Wang, K. An, and L. Cai, "Visualizing the Chemistry and Structure Dynamics in Lithium-ion Batteries by in-situ Neutron Diffraction," *Scientific reports* 2, no. 1 (2012): 1–7, https://doi.org/10.1038/srep00747.

26. X. Cao, H. Jia, W. Xu, and J.-G. Zhang, "Review—Localized High-Concentration Electrolytes for Lithium Batteries," *Journal of The Electrochemical Society* 168, no. 1 (2021): 010522, https://doi.org/10.1149/1945-7111/abd60e.

27. R. Weber, M. Genovese, and A. Louli, "Long Cycle Life and Dendrite-free Lithium Morphology in Anode-free Lithium Pouch Cells Enabled by a Dual-salt Liquid Electrolyte," *Nature Energy* 4, no. 8 (2019): 683–689, https://doi.org/10.1038/s41560-019-0428-9.

28. S. Wang, Y. Wang, and Z. Ouyang, "Molecular Engineering of Two-Dimensional Polyamide Interphase Layers for Anode-Free Lithium Metal Batteries," *Nature Materials* 24, no. 12 (2025): 1957–1967, https://doi.org/10.1038/s41563-025-02339-y.

29. Z. Ouyang, Y. Wang, and S. Wang, "Programmable DNA Interphase Layers for High-Performance Anode-Free Lithium Metal Batteries," *Advanced materials* 36, no. 26 (2024): 2401114, https://doi.org/10.1002/adma.202401114.

30. Y. Zhang, W. Bao, and E. Jeffs, "Unveiling the Impacts of Charge/Discharge Rate on the Cycling Performance of Li-Metal Batteries," *ACS Energy Letters* 10, no. 2 (2025): 872–880, https://doi.org/10.1021/acsenergylett.4c03215.

Supporting Information

Additional supporting information can be found online in the Supporting Information section.

Supporting File: aenm71028-sup-0001-SuppMat.docx.

16146840, 0, Downloaded from https://advanced.onlinelibrary.wiley.com/doi/10.1002/aenm.71028 by University Of Chicago Library, Wiley Online Library on [06/05/2026]. See the Terms and Conditions (https://onlinelibrary.wiley.com/terms-and-conditions) on Wiley Online Library for rules of use; OA articles are governed by the applicable Creative Commons License